



Infrared-active quadruple contrast FePt nanoparticles for multiple scale molecular imaging



Shang-Wei Chou^a, Chien-Liang Liu^a, Tzu-Ming Liu^{b, c, **}, Yu-Fang Shen^{b, c, d}, Lun-Chang Kuo^{b, c}, Cheng-Ham Wu^{b, c}, Tsung-Yuan Hsieh^{b, c}, Pei-Chun Wu^{b, c}, Ming-Rung Tsai^{b, c}, Che-Chang Yang^e, Kai-Yao Chang^e, Meng-Hua Lu^f, Pai-Chi Li^g, Shi-Ping Chen^g, Yu-Hsin Wang^g, Chen-Wen Lu^h, Yi-An Chen^a, Chih-Chia Huangⁱ, Churng-Ren Chris Wang^j, Jong-Kai Hsiao^{h, ***}, Meng-Lin Li^{e, f, ****}, Pi-Tai Chou^{a, *}

^a Department of Chemistry, National Taiwan University, Taipei 10617, Taiwan

^b Institute of Biomedical Engineering, National Taiwan University, Taipei 10617, Taiwan

^c Molecular Imaging Center, National Taiwan University, Taipei 10617, Taiwan

^d 3D Printing Medical Research Center, China Medical University Hospital, Taichung City, Taiwan

^e Department of Electrical Engineering, National Tsing Hua University, Hsinchu 30013 Taiwan

^f Institute of Photonics Technologies, National Tsing Hua University, Hsinchu 30013 Taiwan

^g Department of Electrical Engineering, National Taiwan University, Taipei 10617, Taiwan

^h Department of Medical Imaging, Taipei TzuChi Hospital, The Buddhist Tzuchi Medical Foundation, New Taipei City 23142, Taiwan

ⁱ Department of Photonics, National Cheng Kung University, Tainan 701, Taiwan

^j Department of Chemistry and Biochemistry, National Chung Cheng University, Chia-Yi County 62102, Taiwan

ARTICLE INFO

Article history:

Received 15 January 2016

Accepted 25 January 2016

Available online 27 January 2016

Keywords:

FePt nanoparticle

Infrared-active

Multi-modality contrast

Multiphoton luminescence

Photoacoustic responses

Molecular imaging

ABSTRACT

A single nanomaterial with multiple imaging contrasts and functions is highly desired for multiscale theragnosis. Herein, we demonstrate single 1–1.9 μm infrared-active FePt alloy nanoparticles (FePt NPs) offering unprecedented four-contrast-in-one molecular imaging – computed tomography (CT), magnetic resonance imaging (MRI), photoacoustic (PA) imaging, and high-order multiphoton luminescence (HOMPL) microscopy. The PA response of FePt NPs outperforms that of infrared-active gold nanorods by 3- to 5.6-fold under identical excitation fluence and particle concentrations. HOMPL (680 nm) of an isolated FePt NP renders spatial full-width-at-half-maximum values of 432 nm and 300 nm beyond the optical diffraction limit for 1230-nm and 920-nm excitation, respectively. The *in vivo* targeting function was successfully visualized using HOMPL, PA imaging, CT, and MRI, thereby validating FePt as a single nanomaterial system covering up to four types (Optical/PA/CT/MRI) of molecular imaging contrast, ranging from the microscopic level to whole-body scale investigation.

© 2016 Elsevier Ltd. All rights reserved.

1. Introduction

Molecular imaging has become an indispensable tool for pre-clinical research, clinical trials, and clinical practice in the context of

personalized medicine [1]. With the help of molecular contrast agents, the spatial distribution and dynamics of disease-related molecules or the pharmacokinetics of therapeutics can thus be visualized and quantitatively analyzed *in vivo*. To provide strong contrast and sufficient sensitivity in different imaging modalities, various nanomaterial systems have been developed. Radiolabeled metabolic analogs or ligands were used in positron emission tomography (PET) to diagnose disease-related metabolic disorder or dysfunction of cell-surface receptors [2,3]. Chelates of metal ions or superparamagnetic iron oxides were found to enhance the T_1 and T_2 contrasts in magnetic resonance imaging (MRI) [4–6]. Metal-based nanoparticles enabled the molecular imaging of X-ray computed tomography (CT) [7–9], and their strong surface-

* Corresponding author.

** Corresponding author. Institute of Biomedical Engineering, National Taiwan University, Taipei 10617, Taiwan.

*** Corresponding author.

**** Corresponding author. Department of Electrical Engineering, National Tsing Hua University, Hsinchu 30013, Taiwan.

E-mail addresses: tmliu@ntu.edu.tw (T.-M. Liu), jongkai@tzuchi.com.tw (J.-K. Hsiao), mlli@ee.nthu.edu.tw (M.-L. Li), chop@ntu.edu.tw (P.-T. Chou).

plasmon-resonance (SPR) absorption provided valuable contrast for photoacoustic (PA) imaging [10,11]. Lipid- or albumin-based microbubbles offered a designable template for ultrasound molecular imaging [12,13]. In optical spectroscopy or microscopy, molecular information can be obtained through absorption or luminescence by endogenous pigments, immunofluorescence-labeled antibodies, bio-luminescent probes, transgenically labeled fluorescent proteins, and functionalized quantum dots [14]. Different molecular imaging modalities, however, have their own advantages and disadvantages in terms of sensitivity, spatial-temporal resolution, and imaging depth [1]. To gain a comprehensive understanding of the physiology or pathology of diseases *in vivo*, multi-modal molecular imaging is required for multiscale investigations and proofs of principle. For this purpose, researchers commonly synthesize nanocomposites to achieve multimodal contrasts in single agents [15–17]. Reducing the complexity of the synthesis and the toxicity of the materials demands a single material system that can cover as many types of contrast as possible. For example, the commonly used gold nanomaterial system provides CT contrast [9], SPR absorption for PA imaging [10,11], and two-photon luminescence contrasts [18], thus covering three major imaging modalities (Optical/CT/PA) while unfortunately lacking others such as MR contrast. To date, no single-material system can cover more than three classes of contrast.

Recently, FePt nanoparticles (FePt NPs) have emerged as effective CT/MRI dual-modality imaging agents [7]. Their long-term circulation and targeting capabilities have been successfully demonstrated *in vivo* [7]. In addition, FePt NPs displayed better photothermal efficiency than gold NPs in the near infrared (NIR) wavelength range [19]. This phenomenon implied that FePt NPs might have strong NIR absorption, which could potentially generate PA and/or multiphoton optical contrast. In this report, we further explored the capability of FePt NPs to offer PA and multiphoton optical contrast by evaluating their contrast capabilities in PA and optical modalities with infrared laser-pulse excitation. Interestingly, high-order multiphoton luminescence (HOMPL), including three-photon luminescence (3PL) and four-photon luminescence (4PL), was observed with FePt NPs and exploited to demonstrate the first HOMPL microscopy. We further discovered that FePt NPs produce much stronger PA signals and thus offer potentially deeper imaging depth than infrared-active gold nanorods, a commonly used PA contrast agent. These two valuable types of contrast, in combination with MRI and CT contrast, enable FePt to provide unprecedented quadruple (Optical/PA/CT/MRI) imaging contrast in a single nanomaterial system for imaging from the microscopic level up to whole-body scale investigation.

2. Materials and methods

2.1. Materials

Platinum acetylacetonate ($\text{Pt}(\text{acac})_2$, ACROS, 97%), iron pentacarbonyl ($\text{Fe}(\text{CO})_5$, Aldrich, 99%), hexadecane-1,2-diol (Aldrich, 90%), oleyl amine (ACROS, C18 content 80–90%), oleic acid (Aldrich, 70%), dioctyl ether (Aldrich, 90%), 1-octadecene (ACROS, 90%), 6-mercaptohexanol (Aldrich, 97%), cysteamine (Sigma, 95%), ethyl-3-[3-dimethylaminopropyl] carbodiimide hydrochloride (Aldrich, 98%), N-hydroxysuccinimide (Acros, 98%) and anti-VEGFR antibodies (ebioscience, anti-mouse-cd309 biotin, 500 $\mu\text{g}/\text{mL}$).

2.2. Synthesis and ligand exchange of FePt nanoparticles

As-prepared FePt nanoparticles (~12 nm) were synthesized according to a previous article [7]. The procedure is described as follows: $\text{Pt}(\text{acac})_2$ (195 mg), $\text{Fe}(\text{CO})_5$ (66 μL), 1,2-hexadecandiol

(1.05 g), oleyl amine (4 mL) and oleic acid (4 mL) and dioctyl ether (4 mL) were loaded into a three-neck flask. The chemical mixture in the N_2 atmosphere was heated to 240 °C at a heating rate of 15 °C/min. The reaction temperature was maintained for 60 min, and then the reaction mixture was cooled to room temperature. The black particles were separated by the addition of ethanol followed by centrifugation. The final product was stored in hexane or toluene.

In the procedure of ligand exchange, the dry FePt nanoparticles (~30 mg) were dispersed in ODE by sonication. 6-mercaptohexanol (~600 μL) was mixed into the previous mixture at room temperature. The temperature of the mixture was kept at ~55 °C (heating rate ~ 5 °C/min) overnight. Then the final product was washed to clean the physically adsorbed ligand on the particle surfaces by the addition of methanol and hexane. Finally, the 6-mercaptohexanol-modified FePt nanoparticles (FePt NPs) were collected and stored in a bottle filled with N_2 .

For the anti-VEGFR antibodies conjugation of FePt NPs, FePt NPs were first modified cysteamine through the procedure reported in previous article [7]. Then, FePt NPs with amine group were incubated with ethyl-3-[3-dimethylaminopropyl] carbodiimide hydrochloride (EDC) at 4 °C. After 10 min, the suitable amount of N-hydroxysuccinimide (NHS) was mixed with this solution at 4 °C for 30 min. Finally, the anti-VEGFR antibodies were added into the above solution and then, the mixture was stirred at 4 °C for 8–10 h. The pellets were centrifuged in 10,000 rpm for 10 min and washed in phosphate-buffered saline (PBS) twice before next steps.

2.3. Characterization

Transmission electron microscopy (TEM) images were obtained with a JEOL 1230 transmission electron microscope (at 100 kV). The powder x-ray diffraction scan (PXRD) was performed on a PANalytical X'Pert PRO diffractometer and recorded from 20° to 60°. The FePt nanoparticle powder was deposited on Si wafer, and the workup procedure was carried out with Cu $K\alpha$ radiation ($\lambda = 1.54178 \text{ \AA}$). FTIR spectra in the region of 500–4000 cm^{-1} were collected with a Varian 640-IR spectrometer.

2.4. Multiphoton nonlinear optical microscope with a micro-incubator

The imaging system used was a home-built femtosecond Cr:forsterite-laser-based multiphoton nonlinear optical microscope with a sub-micron 3D spatial resolution. The laser wavelength was set at approximately 1250 nm, which falls in the NIR-penetration window (1200–1300 nm) of most biological tissues. Unlike the commonly used Ti:sapphire laser (700–1000 nm), this laser does not resonantly excite the two-photon Soret band of many endogenous fluorophores in cells and tissues, thereby resulting in less on-focus damage. Due to these advantages, particularly *in vivo* imaging in deep tissues, the Cr:forsterite laser has been widely applied in developmental biology [20] and human clinical studies [21]. Because most of the autofluorescence is suppressed, optical contrast agents that can be efficiently excited at approximately 615 nm should exhibit red emission and thus be beneficial to deep-tissue imaging. The laser beam was XY-scanned by a scanning unit (FV300, Olympus, Japan) cascaded with an inverted microscope (IX71, Olympus, Japan). The laser beam was then transmitted to a multiphoton dichroic beam splitter (edged at 665 nm) and focused by a water immersion objective (1.2 NA, 60 \times , Olympus, Japan). The resulting red multiphoton luminescence, SHG, and THG were epifluorescence collected by the same objective. The red multiphoton luminescence ($\lambda > 665 \text{ nm}$) was transmitted to a dichroic beam splitter and detected by a photomultiplier tube (PMT) in the scanning unit. The

SHG and THG signals were reflected and then separated by another dichroic beam splitter edged at 490 nm and separately detected by two additional PMTs. All three channels were reconstructed into 512×512 images using software in a computer at a 2-Hz frame rate.

For imaging of live cells, a micro-incubator on a microscope was used to create an environment with a temperature of 37 °C and a 5% CO₂/95% air atmosphere. The temperature of the thermostat (LAUDA, Ecoline Staredition RE 204) was set at 50 °C to achieve 37 °C at the distal end of the objective. Vapor that reached the micro-incubator through a duct maintained the micro-incubator at approximately 37 °C. The gas controller (OkO Lab) continuously supplied 5% CO₂ to maintain the absolute outlet pressure at 1 atm. The 1.2 NA water-immersion objective was heated using a dual temperature controller (TC-144, WARNER Instruments). This approach allowed the temperature at the bottom of the dish to be maintained at approximately 37 °C.

2.5. *In vivo* T₂-weighted MR and CT imaging of the mice bearing melanoma tumor

Mice bearing melanoma tumor were anesthetized using 2% isoflurane mixed with 100% O₂ and then, subjected to the two imaging modality analysis after tail-vein injection of anti-VEGFR-FePt NPs. The *in vivo* experiments were performed a clinical 3 T MR system (Signa Excite, GE Healthcare, USA) before and after the injection of anti-VEGFR-FePt NPs. The images were taken at a time sequence from 0 to 1 h using T₂-weighted MR acquisition sequence with the following parameters: fast spin echo with TR/TE = 3000 ms/99.7 ms, ET = 10 ms. Further, the signal intensity of tissue in each test was determined by standard region-of-interest measurements of cross-sectional image of the tissue using the provided image quantification software. The *in vivo* CT analysis was acquired using a GE Light Speed VCT 64-detector CT. Imaging parameters were as follows: slice thickness, 0.625 mm; 120 kVp, 30 mA; field of view, 512×512 , gantry rotation time, 0.4 s; table speed, 40 mm/rotation. The each image acquisition was performed when rotated one step (1°) through 360°. The images were processed for cross sections by reconstruction using analysis software.

2.6. *In vivo* 4PL imaging

C57BL/6-c2J and BALB/c mice at 4–6 weeks old were separately obtained from the laboratory animal center (National Taiwan University College of Medicine, Taiwan) and LASCO (Taiwan) and maintained in the animal research center core facility (National Taiwan University College of Medicine, Taiwan). B16-F10 melanoma cells (American Type Culture Collection [ATCC]; CRL-6322) were obtained from the Food Industry Research and Development Institute (Taiwan). BNL-1 MEA.7R.1 (BNL) mouse hepatocellular carcinoma (HCC) cells were provided by Dr. Da-Liang Ou (National Taiwan University, Taiwan). The mCherry B16F10 stable cell line was established using the Retro-XTM Universal Packaging System (Clontech Laboratories Inc). This system includes the GP2-293 cell line, whose genome incorporates the viral gag and pol genes. B16-F10 melanoma, BNL and mCherry B16F10 melanoma stable cells were grown in Dulbecco's Modified Eagle Medium (DMEM, Invitrogen) containing 4.5 g/L D-Glucose, 10% fetal bovine serum (FBS, Gibco), 2 mM L-glutamine (Invitrogen), and penicillin and streptomycin (100 µg/mL; Invitrogen). The cells were maintained at 37 °C and 5% CO₂. The mCherry B16F10 melanoma stable cells were implanted into the ears of C57BL/6-c2J mice. BALB/c mice were subcutaneously inoculated in the dorsal right flank with 1×10^6 BNL cells. All animal experiments were performed in accordance with animal welfare guidelines and approved by the Institutional Animal Care and Use Committee (IACUC) of National Taiwan

University College of Medicine. Mouse body weights were 25 g at the time of the experiments.

For the static observation of mice via *in vivo* nonlinear microscopy, we used the inhaled anesthetic isoflurane due to its effectiveness, lack of side-effects, and rapid wash-out, especially for consecutive time-course imaging. Isoflurane supplies oxygen during the entire anesthetic period and is good for rapid anesthetic recovery. Anesthesia was induced using vaporized isoflurane at up to 4% and maintained with 0.8–1.5% isoflurane during prolonged experimental observation. We monitored the reflexes and vital signs (94–163 breaths/min, 325–780 beats/min, 37.5 °C) of the anesthetized mouse and maintained the body temperature using a small warm bag during the entire anesthetic period and throughout the recovery period.

2.7. HOMPL and photostability examination of FePt NPs

Four-photon luminescence images of FePt NPs were performed on a Leica TCS SP5 MP equipped with a femtosecond Ti:sapphire laser and an optical parametric oscillator (OPO). The OPO can extend excitation wavelength to 1–1.3 µm. The objective used in imaging was a 20×, 0.75 NA water-immersion objective (Leica). Three-photon excitation at 920 nm and four-photon excitation 1230 nm both resulted in red luminescence signals of the nanoparticles. The average powers after the objective were both 80 mW and the corresponding fields of view were 255 µm × 255 µm with 512×512 pixels. Through statistical analysis of the fluorescence images, we obtained an average intensity for each picture that can be used as a measure of the luminescence intensity. The photostability of the nanoparticles was determined by 8 min continuous excitation with femtosecond laser pulses at wavelengths of 920 nm and 1230 nm. For the *in vivo* evaluation of photostability, the imaging depth under test was 50 µm.

2.8. Evaluation of *in vivo* imaging depth on 3PL of FePt NPs and 2PF of AuNR_{1,000}

The C57BL/6-c2J mice were injected with 50 µL of FePt NPs or AuNR_{1,000} (2 mg/mL) into the subcutaneous regions of the mouse ears. The *in vivo* sectioning images of the nanoparticles were captured on a Leica TCS SP5 MP system equipped with a Ti:sapphire laser and an OPO. The multiphoton excitation wavelength was 920 nm. The objective used in imaging was a 20×, 0.75 NA water-immersion objective (Leica). To evaluate the capability of imaging depth, we acquire sectioning images from 0 to 200 µm deep at a step size of 5 µm.

2.9. Measurement of the PA effect

The sample tubes were immersed in water at a depth of 12 mm and irradiated by 1064 nm pulses from an Nd:YAG laser (LS-2132 U, LOTIS TII, Minsk, Belarus) at a repetition rate of 15 Hz. The pulse duration of the laser was 8 ns, and the fluence was approximately 7 mJ/cm². For acoustic detection, a custom 20-MHz fiber-integrated transducer was used. The signals were sent to a preamplifier (5073PR, Panametrics, Waltham, MA) and recorded by a data acquisition card (CompuScope 14200, Gage, Lachine, QC, Canada) at a sampling rate of 100 MHz. The transducer was mounted on a precision translation stage, and a B-scan image was obtained by moving the driving motor (HR-8, Nanomotion, Yokneam, Israel) at a step size of 50 µm. The recorded data were processed using an offline method. The data were first filtered by a band pass filter to remove the noise and then demodulated with the transducer's central frequency for envelope detection. The PA images were shown with the amplitude displayed with the dynamic range of

55 dB. The maximum-amplitude-projection profile of the PA B-scan images was obtained by projecting the highest value along the depth axis, which was presented on a linear scale.

2.10. *In vivo* PA imaging

For the *in vivo* PA experiments, a 25-MHz dark-field confocal PA microscopy (PAM) system was used. A pulsed Nd:YAG laser system (Surlite II-10, Continuum), with pulse width of 6.5 ns, pulse repetition rate of 10 Hz, and wavelength of 1064 nm, was used to provide laser pulses for PA excitation. The laser energy was uniformly delivered to the region of interest in a dark-field configuration via the optical path, which was composed of an optical fiber, two lenses, an axicon and a plexiglass. The incident energy density on the sample surface was well within the ANSI safety limit, i.e., $<100 \text{ mJ/cm}^2$ at 1064 nm. To receive the PA signals, a 25-MHz focused ultrasound transducer (V324, Olympus) was used, with a -6 dB fractional bandwidth of 55%, a focal length of 12.7 mm, and a 6-mm active element size, thus offering a lateral resolution of 185 μm and an axial resolution of 68 μm . The transducer was immersed in a water tank with a hole at the bottom sealed with a piece of polyethylene membrane. The imaged part of the animal (e.g., the tumor site of the mouse) was coated with a thin layer of ultrasonic gel and then placed below the membrane. After detection by the ultrasonic transducer, the PA signals were pre-amplified by 38 dB with a low-noise amplifier, filtered and re-amplified by a pulser/receiver (5073 PR, Olympus), digitized by an analog-to-digital card (CompuScope 14200, GaGe), and then stored on a personal computer.

Note that the *in vivo* PA B-scan images were taken with signal averaging of 4 times to improve the signal-to-noise ratio, and the brightness of the images corresponded to the amplitude of the detected PA signals. By changing the excitation source from the laser to the ultrasound pulser, the imaging mode could be switched from PAM to ultrasound microscopy, thereby providing complementary structural information with 56- μm axial and 125- μm lateral resolution, respectively. Each ultrasound B-mode image was acquired with signal averaging of 32 times.

Anesthetized mice bearing liver tumors (BNL 1MEA.7R1 liver cancer cell line) and weighing approximately 20 g were used for the *in vivo* experiments. All animal experiments were conducted in accordance with the guidelines from Animal Research Committee of National Taiwan University and National Tsing Hua University, Taiwan. The mice were subcutaneously inoculated with liver cancer cells on the hind dorsal part. Imaging was performed 21 days after tumor inoculation, and the mice were anesthetized by gas anesthesia with isoflurane at a dose of 1% in pure oxygen at a 1-L/min flow rate during the imaging procedure. Body temperature was maintained with a warming lamp and the thermostat in the water tank. Ultrasound and PA pre-scans prior to FePt nanoparticle administration were performed to determine the background signals. A 10-mg/mL dose of FePt nanoparticles in 100 μL was then administered intravenously. After injection, the tumor foci were imaged every 10 min via PAM and monitored for up to 80 min.

3. Results and discussions

Hydrophilic FePt NPs with average sizes of $11.8 \pm 2.05 \text{ nm}$ (Fig. S1) were obtained through modification with 6-mercaptohexanol (note that hereafter, the 6-mercaptohexanol-modified FePt NPs are abbreviated as FePt NPs). Their morphologies and sizes are similar to those of the as-prepared particles (Fig. 1a and Fig. S1a). Fourier Transform Infrared (FTIR) spectra of the as-prepared FePt NPs and FePt NPs revealed the characteristic bands from the adsorbed ligands, including oleic acid, oleyl amine, and 6-

mercaptohexanol, on the surface (Fig. S1b). Additionally, the powder X-ray diffraction (PXRD) results (Fig. S1c) showed that the core structure of FePt NPs was stable after the alteration of the ligand shell. These data, together with good water solubility, ensure the complete and successful execution of the ligand exchange process. In MTT cell toxicity assays (Fig. S2a), FePt NPs demonstrated no significant cytotoxicity ($\geq 80\%$ cell viability) at various particle concentrations. Furthermore, the low hemolysis ($<5\%$) of FePt NPs had been reported [7]. Thus, these results justified the biocompatibility of FePt NPs for further *in vitro* and *in vivo* investigations in this study. *In vitro* time-course images (Fig. S2b) showed that HeLa cells taking up FePt NPs were promptly damaged under a low illumination intensity of 1 mW/cm^2 at 800 nm. By contrast, under a similar light intensity, HeLa cells without FePt NP uptake (left-most in Fig. S2b) survived after a long laser irradiation period (0–280 s). These results not only validate the good photothermal capability of FePt NPs after surface modification but also imply a strong NIR absorption of FePt NPs [19].

To characterize the absorption properties of FePt NPs, sample films were prepared by depositing FePt NPs onto an indium tin oxide (ITO) glass substrate and then dried under vacuum at room temperature overnight. A UV–visible–NIR diffuse reflectance spectrophotometer equipped with an integrating sphere was used to record the absolute absorption characteristics of samples in the wavelength range of 300–1900 nm. Both as-prepared FePt NPs and FePt NPs exhibit apparent infrared absorption bands that increase from 1 μm , reach a plateau at 1.3 μm , and then extend to 1.9 μm (Fig. 1b and Fig. S3c, black curve). In the biological penetration window of 1.2–1.3 μm , the absorbance magnitude is even as large as that in the UV region. A similarly strong near-infrared absorption band was also observed for ligand-modified iron oxides, including $\alpha\text{-Fe}_2\text{O}_3$, $\gamma\text{-Fe}_2\text{O}_3$, and Fe_3O_4 [22–24]. Previous reports validated that the strong infrared absorption band of iron oxides is due to their ligand-iron complex on the surface of particles. In fact, many characterizations of the surface state have demonstrated the presence of iron oxides (Fe^{2+} and Fe^{3+}) on the surface of FePt NPs [25,26]. Furthermore, chemical bonds between the Fe ion and the organic ligands with functional groups, such as carboxyl and thiol, have been shown to form during synthesis and modification [27–29]. For verification, pure Pt NPs were synthesized for absorption measurements. The absorption band in the 1000–1900 nm region was clearly absent for the pure Pt NPs (Fig. S3c, green curve). These results support the notion that the presence of iron oxide and/or ligand-iron complexes on the surface induces the distinctive NIR absorption band of FePt NPs.

Given this prominent infrared absorption, we anticipated that the FePt NPs can greatly enhance multiphoton luminescence through resonant coupling; thus, a femtosecond Cr:forsterite laser operating at approximately 1250 nm was used to explore the multiphoton luminescence properties of FePt NPs. A tightly focused (60 \times Olympus UplanApo, 1.2 NA) excitation leads to broad FePt NP luminescence extending from 500 to 850 nm (Fig. 1c and Fig. S4), with a peak wavelength at approximately 680 nm. Integrating the power spectra, we found that the multiphoton luminescence yield revealed a quartic dependence on the excitation power (Fig. 1d, black). Following excitation at shorter wavelengths of 920 nm and 1100 nm, the results (Fig. 1d, red and 1d, blue) still indicated the nonlinear dependence of the luminescence yields (570–640 nm) on excitation power. At low excitation power, the ensemble-averaged slopes of the best linear fits were 2.6 and 2.7 when the pump wavelengths were 920 nm and 1100 nm, respectively. Therefore, luminescence intensity as a function of excitation power could be 3PL or 4PL (HOMPL) depending on the excitation wavelengths. The tunability of the excitation wavelengths for multiphoton-excited emission in FePt NPs thus provides more

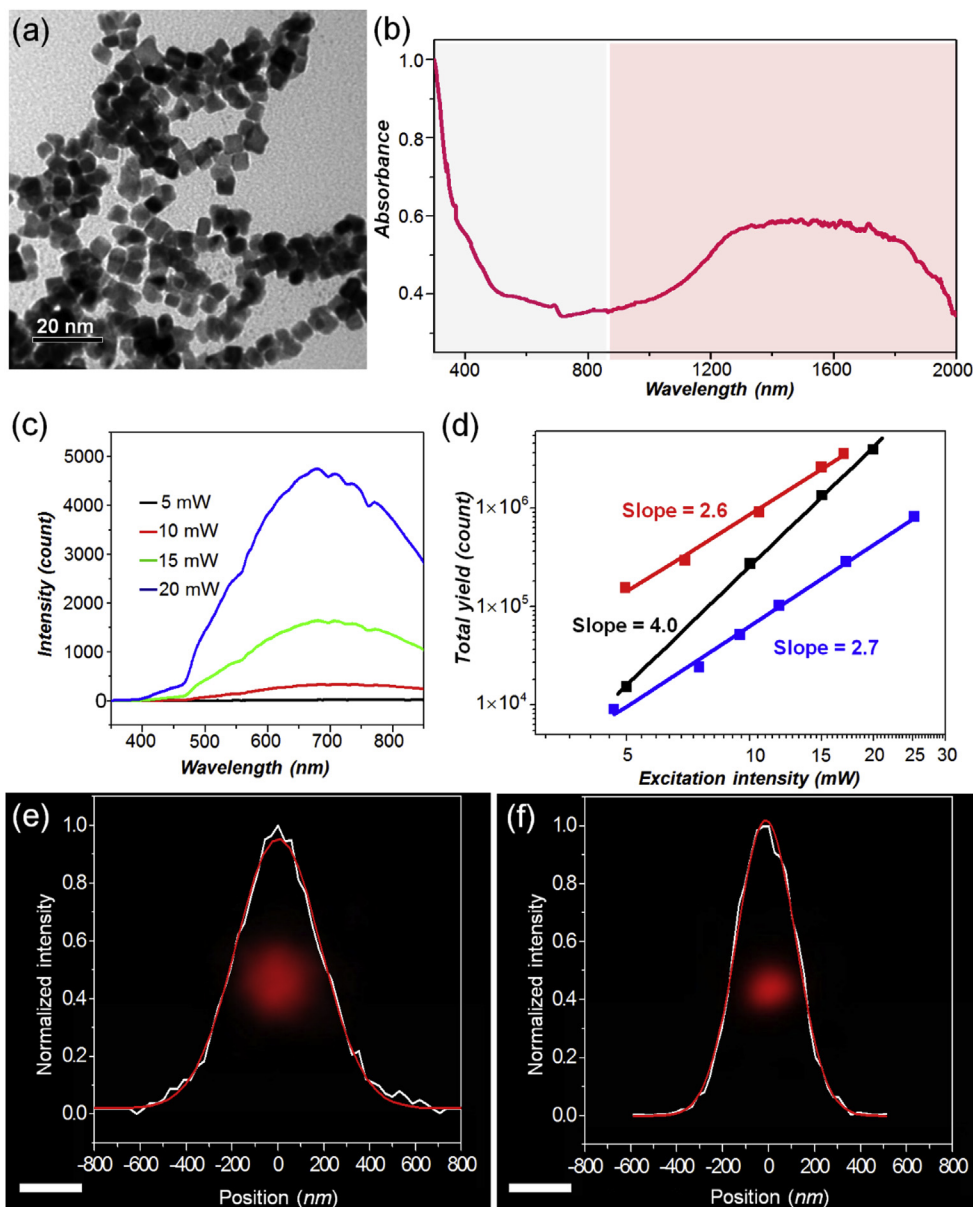


Fig. 1. (a) TEM images obtained from the 6-mercaptohexanol-modified FePt NPs (FePt NPs). (b) UV–visible–NIR absorption spectrum of FePt NPs. (c) Power-dependent multiphoton luminescence spectra of FePt NPs excited at 1250 nm. (d) The total luminescence power versus excitation power at 920 nm (red), 1100 nm (blue) and 1250 nm (black). Curve-fitting of the log–log plot showed slopes of 2.6 for the excitation power at 920 nm, 2.7 for the excitation power at 1100 nm, and 4.0 for the excitation power at 1250 nm. Multiphoton luminescence microscopy of an isolated FePt NP excited at (e) 1230 nm and (f) 920 nm. White curves in (e) and (f) represent the normalized cross-sectional intensity profiles. Red lines depict Gaussian fitting of the white curves. Scale bar of image: 500 nm. (For interpretation of the references to colour in this figure legend, the reader is referred to the web version of this article.)

flexibility for multiple-label biological imaging and medical photodynamic therapy. Despite the prominent multiphoton excitation emission, surprisingly, we could not obtain the single-photon spectrum of FePt NPs (Fig. S5) in water. To ensure the HOMPL can be long-term excited, the photostability of the resulting HOMPL of FePt NPs was also examined both *in vitro* and *in vivo* using laser excitation at 920 nm and 1230 nm. After 8 min of excitation, the magnitude of luminescence did not change significantly (Fig. S6). These results validate that FePt NPs can be used as stable HOMPL labels for long-term cell tracking *in vivo*. This phenomenon was similar to the results reported by Seemann and Kuhn [30]. They found that the single-photon excitation emission of FePt-SiWxOy core/shell NPs was quenched but the multiphoton excitation emission of FePt-SiWxOy was detected in water [30]. Overall,

the pure and single-structural FePt NPs clearly show the high-order non-linearity of PL. The fourth-order dependence of white light luminescence on excitation power was previously reported for a gold nano-antenna fixed on a substrate [31], which was attributed to a three-photon $sp \rightarrow sp$ transition followed by a single-photon $d \rightarrow sp$ absorption [32]. We believe that HOMPL of FePt NPs follows similar carrier dynamics and is resonantly enhanced by the NIR absorption band. The HOMPL contrast of FePt NPs offers several advantages for deep-tissue biomedical microscopy. First, FePt NPs enhance multiphoton excitation at wavelengths that penetrate biological tissues (1–1.3 μm). Second, red to near-infrared luminescence encounters less scattering and hence less attenuation by tissues, substantially increasing the epi-collection efficiency. Moreover, the fourth-order nonlinearity of 4PL is capable of

improving the resolution of microscopy over second- or third-order modalities, which is critical for identifying fine structures, such as the axon or dendrites of a neuron, in deep-tissue multiphoton microscopy [33]. As shown in Fig. 1e and f, an isolated FePt NP was imaged under excitation by 1230-nm (Fig. 1e) and 920 nm (Fig. 1f) femtosecond pulses. The objective used for imaging has 20× magnification and a 0.75 numerical aperture. After Gaussian fitting of their cross-sectional intensity profiles, the FWHM (full-width-at-half-maximum) was found to be 432 nm for 1230-nm excitation (Fig. 1e) and 300 nm for 920-nm excitation (Fig. 1f).

According to Abbe's criterion and considering the nonlinear effects on the FWHM of the point spread function, the lateral resolution of nonlinear optical microscopy can be estimated by:

$$r = \frac{0.5 \times \lambda}{NA \times \sqrt{n}}, \quad (1)$$

where λ is the excitation wavelength, n is the order of nonlinearity, and NA is the numerical aperture of the objective. Accordingly, when the NA of the objective is 0.75, the estimated lateral resolutions of HOMPL microscopy are 410 nm ($n = 4$) and 354 nm ($n = 3$) for 1230-nm and 920-nm excitation, respectively. The 920-nm results exhibited better performance, indicating a HOMPL process for the single particle. Moreover, both of these resolution performances are better than 453 nm, which is the diffraction limit of single-photon fluorescence microscopy at 680 nm using the same objective. In order to compare the performance of HOMPL of FePt NP with other benchmarks, we synthesized gold nanorods with designed SPR at 1 μm (AuNR_{1,000}, Fig. S7a) and quantum dot with the emission peak at 630 nm (QD₆₃₀, Fig. S7d). Conventionally,

owing to the highly efficient two-photon fluorescence (2PF), high two-photon absorption cross section and photostability, the single gold nanorod and QD can be easily observed by 2PF spectroscopy [34–36]. Upon excitation at 920 nm, the resulted single particle images of 2PF (Fig. S7b and S7e) exhibited a resolution of 464 nm for AuNR_{1,000} (Fig. S7c) and 461 nm for QD₆₃₀ (Fig. S7f), which were close to the predicted 434 nm of two-photon excitation ($n = 2$). Obviously, the resolution of HOMPL of FePt NP is superior to that of 2PF for AuNRs (464 nm) and QDs (461 nm). These results indicate that large stoke shift of 3PL and 4PL in FePt nanoparticles can result in the sub-diffraction performance of HOMPL microscopy.

Note that, due to the lack of an efficient 4PL agent, 4PL molecular imaging has not yet been realized in biomedical microscopy. So far, the largest order of nonlinearity for optical contrast is three, such as 3PL and third-harmonic generation (THG). The application of 4PL in biomedical imaging can further improve the spatial resolution of *in vivo* microscopy. Because 4PL from FePt NPs can be efficiently excited by sub-nJ laser pulses, we applied these particles to A549 lung cancer cells and demonstrated for the first time the application of 4PL in biomedical microscopy. In cells taking up FePt NPs, strong red ($\lambda > 665$ nm) luminescence (Fig. 2a and b, yellow) and THG (Fig. 2a, magenta) contrasts were observed at a low (20 mW) and harmless excitation level. The shapes of the cells were clearly depicted with these FePt NPs without photo-damage. Under the same excitation conditions, cells without FePt NPs did not exhibit luminescence in the red wavelength range and lacked THG signals. The cells showed weak intrinsic THG contrast, even when the excitation power was increased to 80 mW (Fig. 2c).

Next, the 4PL and THG signals of FePt NPs were studied to determine their appropriateness for *in vivo* applications. Using a

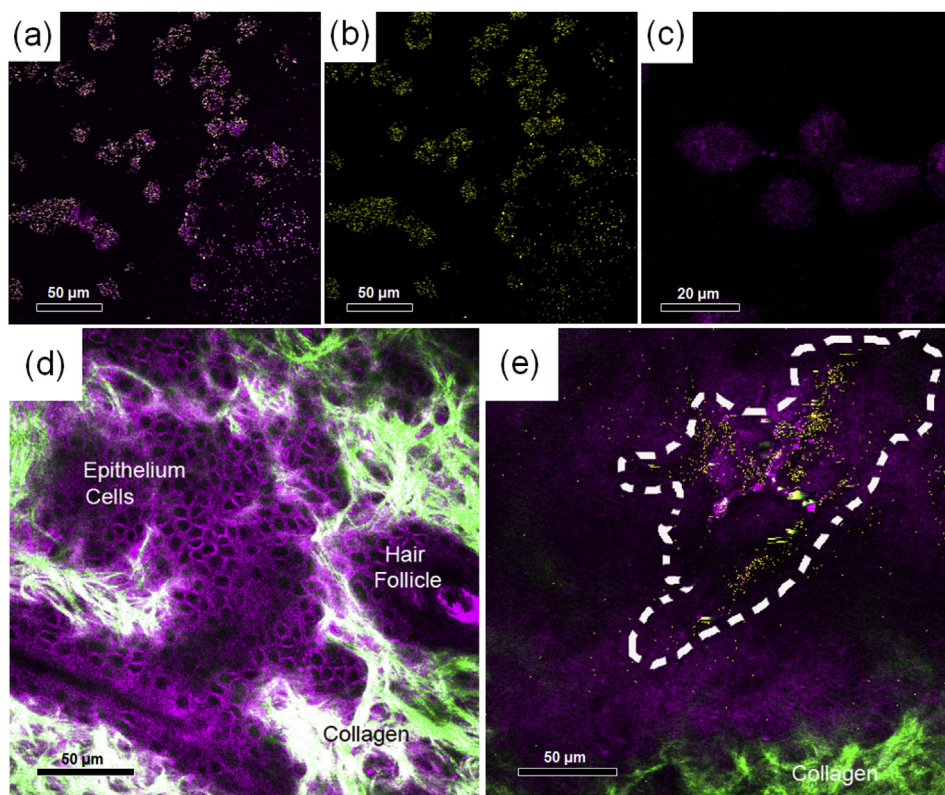


Fig. 2. (a) Combined 4PL (yellow) and THG (magenta) images of A549 cells loaded with FePt NPs. (b) The 4PL image corresponding to (a). (c) Combined 4PL (yellow) and THG (magenta) image of A549 cells without FePt NPs. Fields of view: (a), (b) 240 $\mu\text{m} \times 240 \mu\text{m}$. (c) 80 $\mu\text{m} \times 80 \mu\text{m}$. *In vivo* SHG (green), THG (magenta), and 4PL (yellow) imaging of (d) normal and (e) FePt NP-administered mice ears. The white-dashed contour highlights the region containing FePt NPs. Field of view: 240 $\mu\text{m} \times 240 \mu\text{m}$. (For interpretation of the references to colour in this figure legend, the reader is referred to the web version of this article.)

1250-nm femtosecond laser-based nonlinear optical microscope, we observed the collagen network through second-harmonic generation (SHG) contrast and resolved epithelial cells via THG contrast in mouse ears (Fig. 2d). After subcutaneous administration of FePt NPs in mouse ears, the particle distribution could be clearly observed (Fig. 2e, highlighted by white-dashed contour). Bright luminescence signals were detected in both the SHG (Fig. 2e, green) and red luminescence (Fig. 2e, yellow) channels.

With the success in achieving HOMPL optical contrast, we further investigated the contrast capability of FePt NPs in PA imaging. When combined with acoustic detection of the optical-absorption-induced PA waves, PA imaging can reportedly achieve a 7-cm imaging depth with 720- μm spatial resolution in the diffusive photon regime, and with the help of optical focusing, the spatial resolution can be as good as that of optical microscopy [37]. PA imaging is an imaging modality that can span the microscopic to the whole-body scale.³⁵ Highly absorptive metallic nanoparticles are good candidates for PA contrast agents [10,11]. For deep-tissue PA applications, nanomaterials must possess strong optical absorption in the NIR wavelength range. The distinctive NIR absorption of FePt NPs may provide valuable contrast in NIR PA imaging. As a fair comparison of PA performance, we chose gold nanorods with designed SPR at 1 μm (AuNR_{1,000}) as a benchmark. Both AuNR_{1,000} and FePt NPs were prepared at different mass concentrations and were separately injected into 1-mm diameter polyethylene tubes for PA evaluation. Given the same mass

concentration and excitation fluence, FePt NPs produced higher PA signals than AuNR_{1,000} at 1064-nm excitation (see Fig. 3 and Fig. S8). The corresponding improvement factors at various concentration levels ranged from 3 to 5.6-fold.

The above results confirm that infrared-active FePt NPs are endowed with quadruple contrasts (Optical/PA/CT/MRI) for multi-scale molecular imaging. To validate the potential for exploiting these contrasts to map the targeting efficacy of nanomedicines, we further performed *in vivo* quadruple-modality imaging in mice with implanted tumors. In this approach, we prepared FePt NPs conjugated with anti-VEGFR (vascular endothelial growth factor receptor) monoclonal antibody, as illustrated in Fig. 4a [38]. Because the expression level of VEGFR was relatively high in endothelial cells of vessels penetrating or adjacent to tumors compared to those of normal blood vessels, anti-VEGFR antibody-conjugated FePt NPs (anti-VEGFR-FePt NPs) can thus serve as contrast agents to evaluate targeting efficacy [39,40]. As a first step, *in vivo* MRI T₂ and CT images were acquired after *iv* injection (5 mg/mL concentration, 200 μL) for large-scale investigation. Images (Fig. 4) were acquired both before (0 h) and 1 h after injection (1 h). The tumor positions indicated by red circles were analyzed quantitatively. Compared with the MR images before injection, a significant 17% reduction in the intensity of the tumor regions was observed one hour after injection (Fig. 4b and c), concomitant with a significant 113% contrast enhancement in the CT images of the tumor regions (Fig. 4d and e). The MRI T₂ and CT imaging

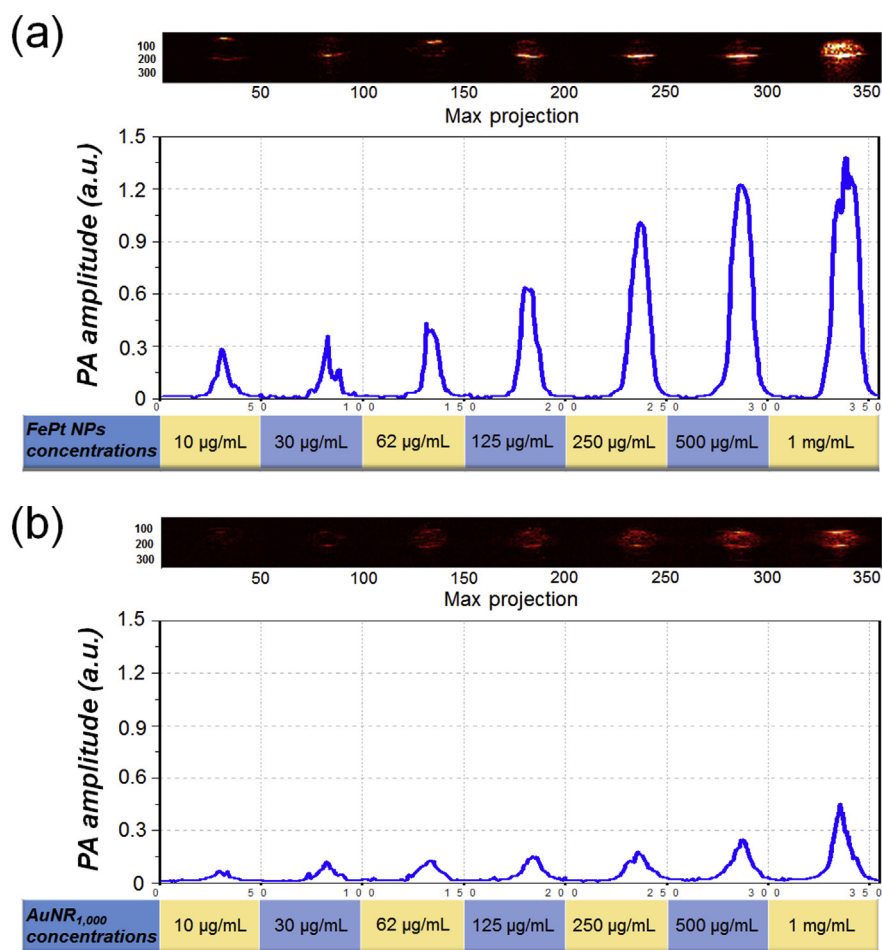


Fig. 3. Photoacoustic images and the maximum-amplitude-projection profiles of (a) FePt NPs and (b) gold nanorods (AuNR_{1,000}) at different concentrations from 10 $\mu\text{g/mL}$ to 1 mg/mL. (For interpretation of the references to colour in this figure legend, the reader is referred to the web version of this article.)

demonstrated that our anti-VEGFR-FePt NPs can selectively target tumor lesions after intravenous administration. Upon closer examination using *in vivo* multiphoton microscopy, at 10 min post injection (5 mg/mL concentration, 200 μ L), the anti-VEGFR-FePt NPs were observed to successfully overcome the biological barriers (Fig. 5a, yellow, 4PL) and specifically target the mCherry-labeled melanoma cells (Fig. 5a, red, two-photon fluorescence, 2PF), which also exhibited 3PL with negligible quenching (Fig. S6c). When the melanoma grew from 1 mm to 5 mm in size, the transvascular targeting efficacies were clearly increased, indicating the enhanced permeation and retention features of tumor microenvironments. In stark contrast, no 4PL signals were observed in the non-tumor region of mouse ears. To compare the imaging depths of FePt NPs and AuNR_{1,000}, we injected each type of nanoparticle into the subcutaneous regions of mouse ears and reconstructed their 3D distribution (Fig. 5b and c). The results (Fig. 5d) showed that FePt NPs were detectable at a depth of 175 μ m (Fig. 5b), which is comparable with that of AuNR_{1,000} (195 μ m, Fig. 5c).

For *in vivo* imaging, the HOMPL contrast of FePt can provide the evaluation of microscopic pharmacokinetics of nanomedicines. Taking our *in vivo* experiments as an example, we treated FePt NPs as drug carriers and used HOMPL imaging to validate the extravasation (permeation out of vessels) as well as the targeting efficacy of carriers on the melanoma cells. The permeation and diffusion dynamics can also reveal the tumor microenvironment, including the tumor associated neovasculatures and the remodeled collagens. Commonly, HOMPL microscopy allowed scanning, sectioning and the reduction of photo-toxicity [41–43]. Also, HOMPL microscopy was less sensitive to light scattering than single-photon microscopy due to infrared excitation, and nonlinear absorption [39,40]. Thus, the combination of HOMPL and organic (synthetic functional fluorescent dyes) or inorganic (nanoparticles) contrast agents was one of the most important imaging-techniques with optical resolution in biology [30,43,44]. However, the depth limit of HOMPL

depended on the spatial and temporal distribution of excitation light, the effective NA, the sample's staining and scattering properties. Especially, the use of higher-order multiphoton excitation could make the depth limit more significant due to the increase in the scattering mean-free path at longer wavelengths [45,46]. Commonly, the signals of HOMPL were weaker than that of single-photon and two-photon microscopy. Nevertheless, the repeated exposure of laser with higher power density could lead to photobleaching and photodamage during the HOMPL measurement [41,47,48]. Therefore, the employment of HOMPL contrast agents facilitated the spatial and temporal resolution, the irradiation penetration depth, and the signal-tracking of single biomolecule [30,43,48,49].

Fig. 6b shows the co-registration results of ultrasound and PA images acquired before injection and different time points after tail-vein injection of anti-VEGFR-FePt NPs (10 mg/mL concentration, 100 μ L) to mice bearing liver tumors (see Fig. 6a for the scanning head of the PA microscopy system used for this study). Compared with the pre-injection PA image, the PA signals acquired after tail-vein injection of anti-VEGFR-FePt NPs became incrementally visible with time. As a result, the PA signal enhancement is significant 60–80 min post injection. The average PA signals from tumor regions with anti-VEGFR-FePt NPs are summarized in Fig. 6c and Table S1 (see supplementary data), which clearly reveals the increasing PA signal as a function of time. Conversely, the average PA signals showed negligible changes and hence remained steady for tumors without anti-VEGFR-FePt NPs (see Fig. S9). These distinct results (Figs. 6b, 6c and S9) affirm the specificity of the anti-VEGFR-FePt NPs in targeting tumor issue, leading to a significant enhancement of *in vivo* PA imaging. Importantly, the PA signals obtained at 60–80 min post injection are ~2-fold higher than those obtained before the injection of anti-VEGFR-FePt NPs. To obtain histopathological evidence of the targeting, we prepared tumor slice-through cryostat sections immediately after the *in vivo* PA

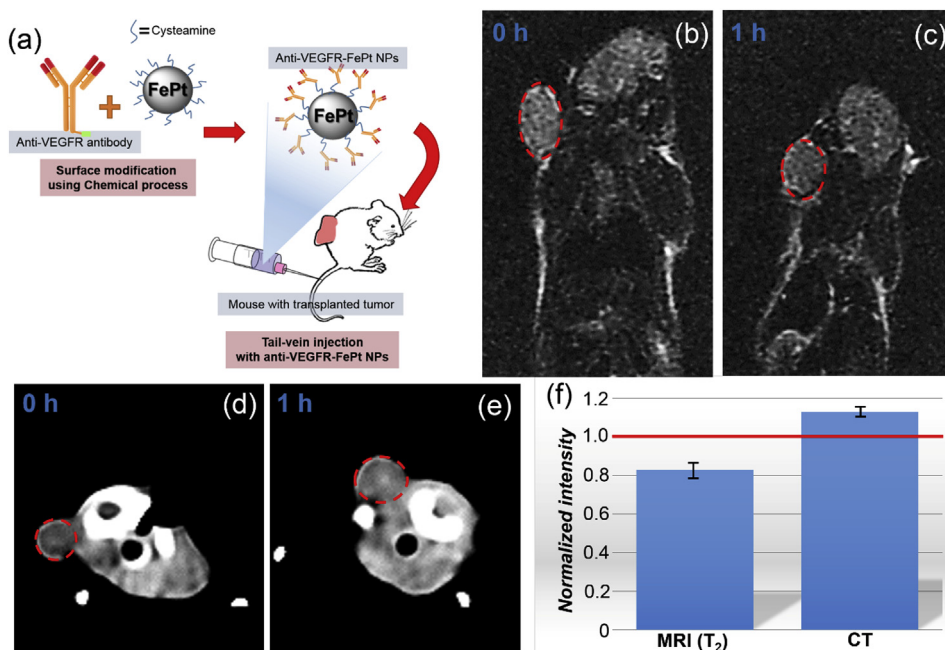


Fig. 4. (a) Illustration of anti-VEGFR antibody conjugated with FePt NPs and tail-vein injection of anti-VEGFR-FePt NPs. The details described in methods and supplemental section. T₂-weighted MR images of the mice bearing melanoma tumor (as indicated by red circles) following tail-vein injection of anti-VEGFR-FePt NPs obtained at (b) 0 h (before injection) and (c) 1 h after injection, respectively. The CT images of the mice bearing melanoma tumor (as indicated red circles) at (d) 0 h (before injection) and (e) 1 h after injection, respectively. (f) The evaluation of the acquired image signal intensity after tail-vein injection of anti-VEGFR-FePt NPs in the tumor area under both MRI and CT is illustrated. Note: the signal intensities of tumor in T₂-weighted MR images and CT images before tail-vein injection are normalized to 1.0 highlighted by a red line. (For interpretation of the references to colour in this figure legend, the reader is referred to the web version of this article.)

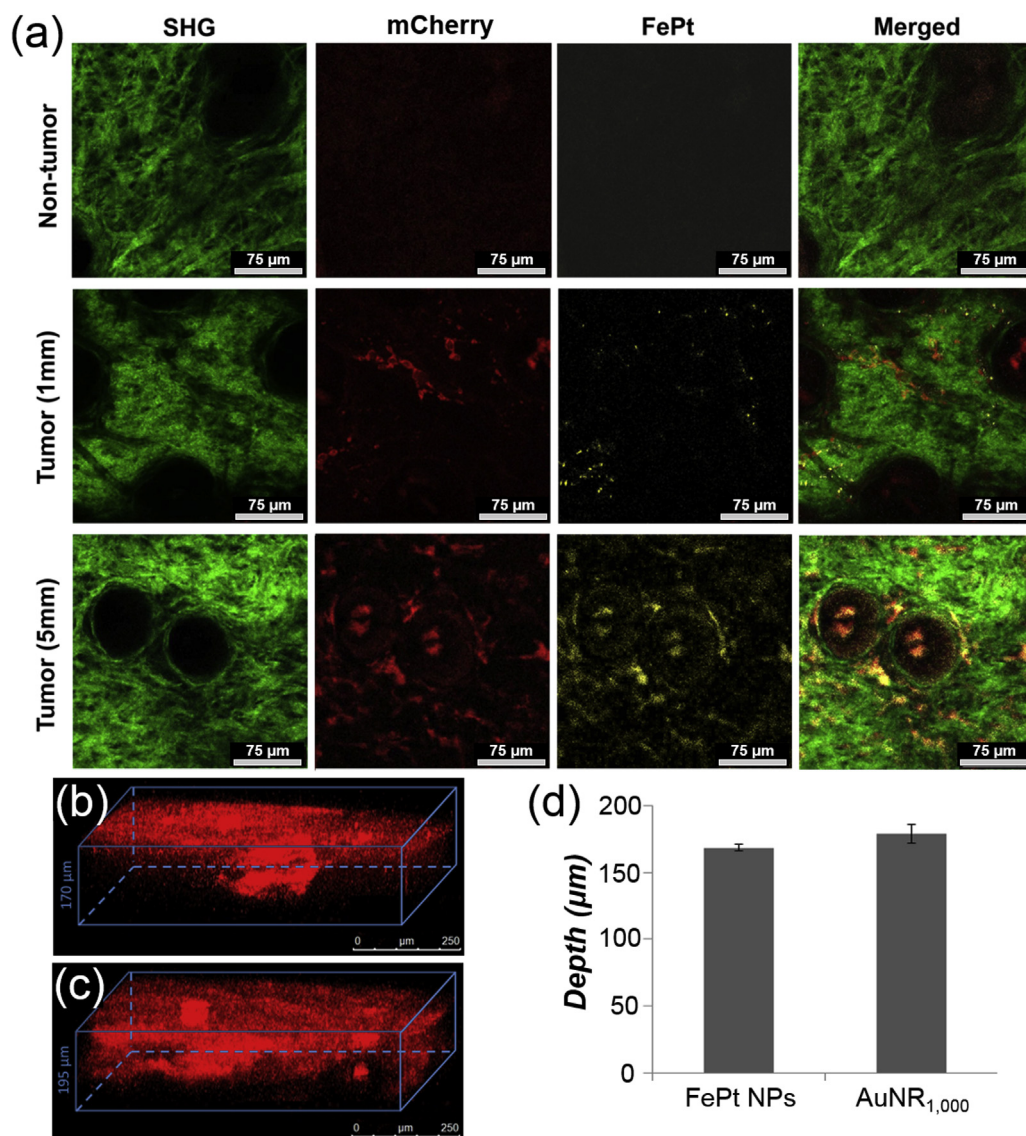


Fig. 5. mCherry 2PF (red), FePt NPs 4PL (yellow), and SHG (green) images of non-tumor and tumor models which were tail-vein injected with anti-VEGFR-FePt NPs. The tumor cells stably expressed mCherry (red). In 5-mm sized tumor images, two sebaceous glands (dark holes in SHG images) with hair follicles emitted 2PF that overlapped with the mCherry and FePt signals. The imaging penetration depth z of ear pinna was 50 μm . Scale bar: 75 μm for all images. Field of view: 255 $\mu\text{m} \times 255 \mu\text{m}$. Reconstructed 3D (b), 3PL and (c) 2PF images of (b) FePt NPs and (c) AuNR_{1,000} in the subcutaneous regions of mouse ears. The corresponding imaging depths ranged from 0 to 170 μm and from 0 to 195 μm . (d) The statistical imaging depth (μm) of FePt NPs and AuNR_{1,000}. (For interpretation of the references to colour in this figure legend, the reader is referred to the web version of this article.)

study. The 3PL image (Fig. 6d) showed bright luminescence signals in both the SHG (Fig. 6d, green) and red luminescence (Fig. 6d, red) at 920-nm excitation. The red luminescence of the FePt NPs demonstrates the specific binding of anti-VEGFR-FePt NPs and the particle distribution in tumor issue. Moreover, AuNR₁₀₀₀ and FePt NPs with the same concentration (2 mg/mL, 50 μL) were subcutaneously injected into the mouse back, respectively, for a fair comparison. The results (Fig. S10) clearly showed that FePt NPs provided higher PA signal in the mouse back tissue.

Overall, the comparison of CT/MRI/PA/HOMPL capabilities of FePt NPs and AuNRs was summarized in Fig. S11. Obviously, FePt NPs exhibited superior resolution and comparable depth for HOMPL, a better signal intensity for PA imaging, and intrinsic MRI T_2 imaging (Fig. S11 and S12). Alternatively, the CT contrast performance of AuNRs was better than that of FePt NPs both *in vitro* and *in vivo* (Fig. S11 and S13) due to the higher X-ray absorption coefficients for Au [7,9].

4. Conclusions

The above results demonstrate that FePt NPs not only display contrast in macroscopic CT/MRI modalities but also show strong responses in mesoscopic PA imaging and microscopic nonlinear optical imaging. The distinctive infrared absorption of FePt NPs resonantly enhances HOMPL contrasts in both *in vitro* and *in vivo* microscopy. Fourth-order nonlinearity and large Stokes-shifted emission allow the resolution of HOMPL microscopy to exceed the diffraction limit. The wavelength tunability of HOMPL enhances multi-color labeled nonlinear optical microscopy. The infrared absorption bands of FePt NPs also provide much better PA performance than that of gold nanorods at its SPR wavelengths. These two new types of contrast demonstrate the ability of FePt NPs to act as a contrast agent for quadruple-contrast multiscale molecular imaging. A single nanomaterial system having quadruple-contrast capability will allow for more flexibility and versatility in the

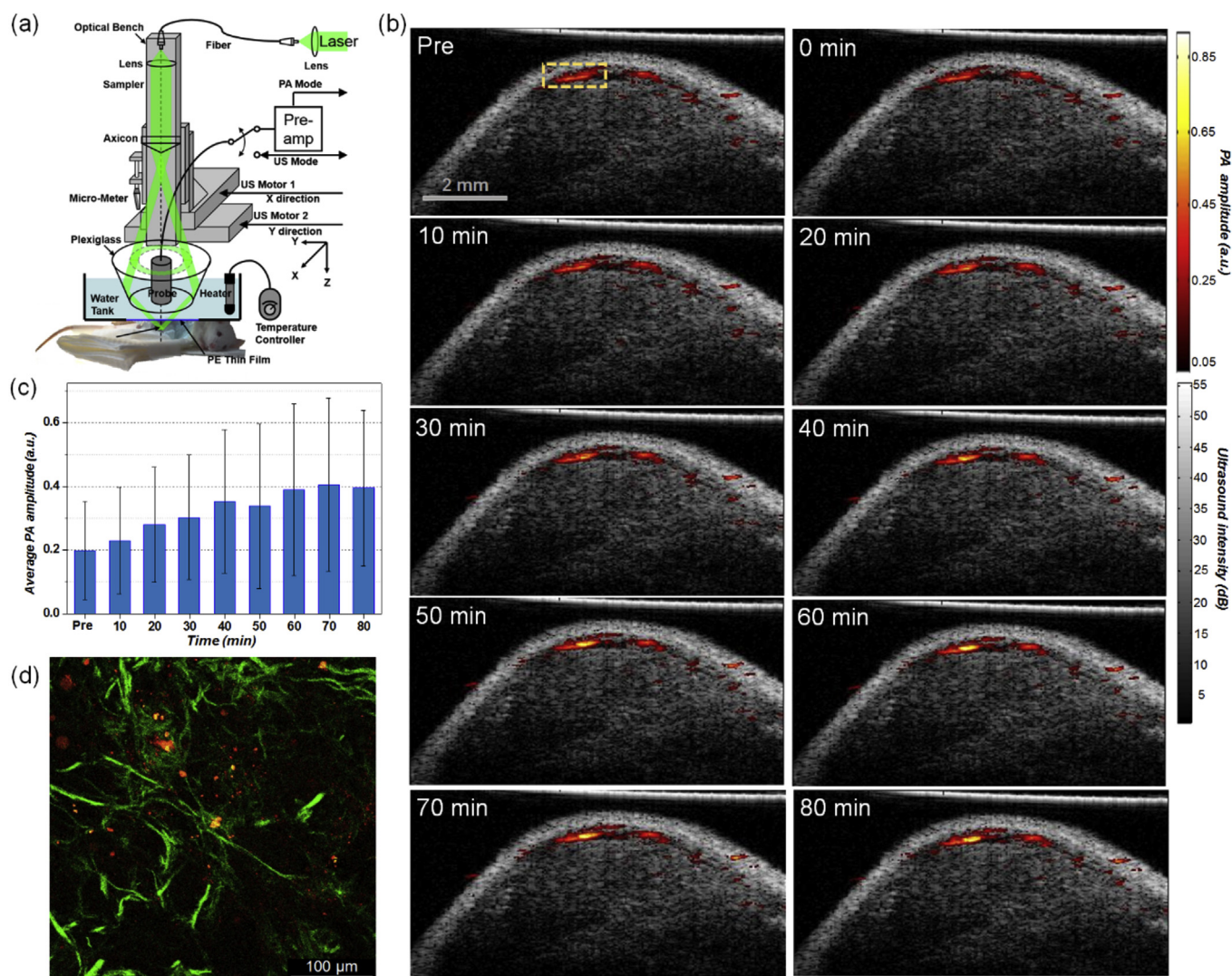


Fig. 6. (a) Schematic diagram of the scanning-head of the 25-MHz dark-field confocal PAM system used for the *in vivo* experiments. For details of the setup, please see the experimental section. (b) The co-registered images of ultrasound and PA images acquired before injection and 0–80 min post injection of anti-VEGFR-FePt NPs. The ultrasound images are displayed in grayscale; the superimposed 1064-nm PA images are displayed with pseudocoloring. (c) Average PA amplitude in the tumor region indicated by the yellow dashed box in (b) as a function of time post injection of anti-VEGFR-FePt NPs. Pre: pre-injection. (d) 3PL image of the tumor slice obtained at an excitation wavelength of 920 nm, which combined images of FePt NPs (3PL, red) and collagen (SHG, green) in the tumor issue. (For interpretation of the references to colour in this figure legend, the reader is referred to the web version of this article.)

design of probes for molecular imaging. Combined with their efficient photothermal effects (better than AuNRs) and significant magnetothermal effect, FePt NPs could be used to simultaneously implement both seamless diagnosis and non-invasive therapy [7,18,50]. As a result, both spatial resolution and target sensitivity can be strategically integrated into FePt nanomaterial systems. FePt nanomaterial systems are thus paving the way for the use of theragnosis agents in deep tissues along with multi-contrast molecular imaging at different scales.

Declaration of interest

The authors declare no competing financial interests.

Acknowledgment

This project is funded by Ministry of Science and Technology of Taiwan, National Health Research Institute of Taiwan (NHRI grant

number: NHRI-EX103-10137E1), and supported by Molecular Imaging Center, National Taiwan University. We are grateful for the help of MRI/CT image acquiring from I-Jou Lin in Department of medical imaging, Taipei TzuChi Hospital. Also, we are appreciative of the supporting of cryostat sectioning from Wei-Hong Wang and Prof. Lin, Sung-Jan in Institute of Biomedical Engineering & Department of Dermatology, National Taiwan University.

Appendix A. Supplementary data

Supplementary data related to this article can be found at <http://dx.doi.org/10.1016/j.biomaterials.2016.01.053>.

References

- [1] R. Weissleder, M.J. Pittet, Imaging in the era of molecular oncology, *Nature* 452 (2008) 580–589.
- [2] P. Som, H.L. Atkins, D. Bandyopadhyay, J.S. Fowler, R.R. Macgregor, K. Matsui, et al., A fluorinated glucose analog, 2-fluoro-2-deoxy-D-glucose (F-18) - nontoxic tracer for rapid tumor-detection, *J. Nucl. Med.* 21 (1980) 670–675.

- [3] G.J. Wang, N.D. Volkow, J. Logan, N.R. Pappas, C.T. Wong, W. Zhu, et al., Brain dopamine and obesity, *Lancet* 357 (2001) 354–357.
- [4] P. Caravan, J.J. Ellison, T.J. McMurry, R.B. Lauffer, Gadolinium(III) chelates as MRI contrast agents: structure, dynamics, and applications, *Chem. Rev.* 99 (1999) 2293–2352.
- [5] R. Weissleder, G. Elizondo, J. Wittenberg, C.A. Rabito, H.H. Bengel, L. Josephson, Ultrasound superparamagnetic iron-oxide - characterization of a new class of contrast agents for MRI imaging, *Radiology* 175 (1990) 489–493.
- [6] J.H. Lee, Y.M. Huh, Y. Jun, J. Seo, J. Jang, H.T. Song, et al., Artificially engineered magnetic nanoparticles for ultra-sensitive molecular imaging, *Nat. Med.* 13 (2007) 95–99.
- [7] S.W. Chou, Y.H. Shau, P.C. Wu, Y.S. Yang, D.B. Shieh, C.C. Chen, In vitro and in vivo studies of FePt nanoparticles for dual modal CT/MRI molecular imaging, *J. Am. Chem. Soc.* 132 (2010) 13270–13278.
- [8] O. Rabin, J.M. Perez, J. Grimm, G. Wojtkiewicz, R. Weissleder, An X-ray computed tomography imaging agent based on long-circulating bismuth sulphide nanoparticles, *Nat. Mater.* 5 (2006) 118–122.
- [9] D. Kim, S. Park, J.H. Lee, Y.Y. Jeong, S. Jon, Antibiofouling polymer-coated gold nanoparticles as a contrast agent for in vivo x-ray computed tomography imaging, *J. Am. Chem. Soc.* 129 (2007) 7661–7665.
- [10] Y.W. Wang, X.Y. Xie, X.D. Wang, G. Ku, K.L. Gill, D.P. O'Neal, et al., Photoacoustic tomography of a nanoshell contrast agent in the in vivo rat brain, *Nano Lett.* 4 (2004) 1689–1692.
- [11] P.C. Li, C.R.C. Wang, D.B. Shieh, C.W. Wei, C.K. Liao, C. Poe, et al., In vivo photoacoustic molecular imaging with simultaneous multiple selective targeting using antibody-conjugated gold nanorods, *Opt. Express* 16 (2008) 18605–18615.
- [12] F.S. Villanueva, W.R. Wagner, Ultrasound molecular imaging of cardiovascular disease, *Nat. Clin. Pract. Cardiovasc. Med.* 5 (2008) S26–S32.
- [13] A.H. Liao, S.Y. Wu, H.E. Wang, C.H. Weng, M.F. Wu, P.C. Li, Evaluation of F-18-labeled targeted perfluorocarbon-filled albumin microbubbles as a probe for microUS and microPET in tumor-bearing mice, *Ultrasonics* 53 (2013) 320–327.
- [14] W.C.W. Chan, S.M. Nie, Quantum dot bioconjugates for ultrasensitive non-isotopic detection, *Science* 281 (1998) 2016–2018.
- [15] Y. Sun, X.J. Zhu, J.J. Peng, F.Y. Li, Core-shell lanthanide upconversion nanophosphors as four-modal probes for tumor angiogenesis imaging, *ACS Nano* 7 (2013) 11290–11300.
- [16] W.P. Li, P.Y. Liao, C.H. Su, C.S. Yeh, Formation of oligonucleotide-gated silica shell-coated Fe₃O₄-Au core-shell nanotrisoctahedra for magnetically targeted and near-infrared light-responsive theranostic platform, *J. Am. Chem. Soc.* 136 (2014) 10062–10075.
- [17] T. Liu, S.X. Shi, C. Liang, S.D. Shen, L. Cheng, C. Wang, et al., Iron oxide decorated MoS₂ nanosheets with double PEGylation for chelator-free radio labeling and multimodal imaging guided photothermal therapy, *ACS Nano* 9 (2015) 950–960.
- [18] H.F. Wang, T.B. Huff, D.A. Zweifel, W. He, P.S. Low, A. Wei, et al., In vitro and in vivo two-photon luminescence imaging of single gold nanorods, *Proc. Natl. Acad. Sci. U. S. A.* 102 (2005) 15752–15756.
- [19] C.L. Chen, L.R. Kuo, S.Y. Lee, Y.K. Hwu, S.W. Chou, C.C. Chen, et al., Photothermal cancer therapy via femtosecond-laser-excited FePt nanoparticles, *Biomaterials* 34 (2013) 1128–1134.
- [20] C.K. Sun, S.W. Chu, S.Y. Chen, T.H. Tsai, T.M. Liu, C.Y. Lin, et al., Higher harmonic generation microscopy for developmental biology, *J. Struct. Biol.* 147 (2004) 19–30.
- [21] S.Y. Chen, S.U. Chen, H.Y. Wu, W.J. Lee, Y.H. Liao, C.K. Sun, In vivo virtual biopsy of human skin by using noninvasive higher harmonic generation microscopy, *IEEE J. Sel. Top. Quantum Electron.* 16 (2010) 478–492.
- [22] T. Hashimoto, T. Yamada, T. Yoko, Third-order nonlinear optical properties of sol-gel derived alpha-Fe₂O₃, gamma-Fe₂O₃, and Fe₃O₄ thin films, *J. Appl. Phys.* 80 (1996) 3184–3190.
- [23] G. Chatzilyriakos, K. Iliopoulos, A. Bakandritsos, S. Couris, Nonlinear optical properties of aqueous dispersions of ferromagnetic gamma-Fe₂O₃ nanoparticles, *Chem. Phys. Lett.* 493 (2010) 314–318.
- [24] M.Y. Liao, C.H. Wu, P.S. Lai, J.S. Yu, H.P. Lin, T.M. Liu, et al., Surface state mediated NIR two-photon fluorescence of iron oxides for nonlinear optical microscopy, *Adv. Funct. Mater.* 23 (2013) 2044–2051.
- [25] H.G. Boyen, K. Fauth, B. Stahl, P. Ziemann, G. Kastle, F. Weigl, et al., Electronic and magnetic properties of ligand-free FePt nanoparticles, *Adv. Mater.* 17 (2005) 574.
- [26] B. Stahl, N.S. Gajbhiye, G. Wilde, D. Kramer, J. Ellrich, M. Ghafari, et al., Electronic and magnetic properties of monodispersed FePt nanoparticles, *Adv. Mater.* 14 (2002) 24–27.
- [27] H.G. Bagaria, E.T. Ada, M. Shamsuzzoha, D.E. Nikles, D.T. Johnson, Understanding mercapto ligand exchange on the surface of FePt nanoparticles, *Langmuir* 22 (2006) 7732–7737.
- [28] Y. Tanaka, S. Saita, S. Maenosono, Influence of surface ligands on saturation magnetization of FePt nanoparticles, *Appl. Phys. Lett.* (2008) 92.
- [29] N. Shukla, C. Liu, P.M. Jones, D. Weller, FTIR study of surfactant bonding to FePt nanoparticles, *J. Magn. Mater.* 266 (2003) 178–184.
- [30] K.M. Seemann, B. Kuhn, Multi-photon excited luminescence of magnetic FePt core-shell nanoparticles, *Biomed. Opt. Express* 5 (2014) 2446–2457.
- [31] P. Muhlschlegel, H.J. Eisler, O.J.F. Martin, B. Hecht, D.W. Pohl, Resonant optical antennas, *Science* 308 (2005) 1607–1609.
- [32] P. Biagioni, D. Brida, J.S. Huang, J. Kern, L. Duo, B. Hecht, et al., Dynamics of four-photon photoluminescence in gold nanoantennas, *Nano Lett.* 12 (2012) 2941–2947.
- [33] N.G. Horton, K. Wang, D. Kobat, C.G. Clark, F.W. Wise, C.B. Schaffer, et al., In vivo three-photon microscopy of subcortical structures within an intact mouse brain, *Nat. Photonics* 7 (2013) 205–209.
- [34] H.F. Wang, T.B. Huff, D.A. Zweifel, W. He, P.S. Low, A. Wei, et al., In vitro and in vivo two-photon luminescence imaging of single gold nanorods, *Proc. Natl. Acad. Sci. U. S. A.* 102 (2005) 15752–15756.
- [35] P. Zijlstra, J.W.M. Chon, M. Gu, Five-dimensional optical recording mediated by surface plasmons in gold nanorods, *Nature* 459 (2009) 410–413.
- [36] D.R. Larson, W.R. Zipfel, R.M. Williams, S.W. Clark, M.P. Bruchez, F.W. Wise, et al., Water-soluble quantum dots for multiphoton fluorescence imaging in vivo, *Science* 300 (2003) 1434–1436.
- [37] L.H.V. Wang, S. Hu, Photoacoustic tomography: in vivo imaging from organelles to organs, *Science* 335 (2012) 1458–1462.
- [38] D.J. Hicklin, L.M. Ellis, Role of the vascular endothelial growth factor pathway in tumor growth and angiogenesis, *J. Clin. Oncol.* 23 (2005) 1011–1027.
- [39] L.F. Brown, B. Berse, R.W. Jackman, K. Tognazzi, E.J. Manseau, D.R. Senger, et al., Expression of vascular-permeability factor (vascular endothelial growth-factor) and its receptors in adenocarcinomas of the gastrointestinal-tract, *Cancer Res.* 53 (1993) 4727–4735.
- [40] K. Weindel, J.R. Moringlane, D. Marme, H.A. Weich, Detection and quantification of vascular endothelial growth-factor vascular-permeability factor in brain-tumor tissue and cyst fluid - the key to angiogenesis, *Neurosurgery* 35 (1994) 439–448.
- [41] K. Konig, Multiphoton microscopy in life sciences, *J. Microsc. Oxford* 200 (2000) 83–104.
- [42] H. Mojzisoava, J. Vermot, When multiphoton microscopy sees near infrared, *Curr. Opin. Genet. Dev.* 21 (2011) 549–557.
- [43] L. Tong, C.M. Cobley, J.Y. Chen, Y.N. Xia, J.X. Cheng, Bright three-photon luminescence from gold/silver alloyed nanostructures for bioimaging with negligible photothermal toxicity, *Angew. Chem. Int. Ed.* 49 (2010) 3485–3488.
- [44] F.E. Hernandez, K.D. Belfield, I. Cohanoschi, M. Balu, K.J. Schafer, Three- and four-photon absorption of a multiphoton absorbing fluorescent probe, *Appl. Opt.* 43 (2004) 5394–5398.
- [45] P. Theer, W. Denk, On the fundamental imaging-depth limit in two-photon microscopy, *J. Opt. Soc. Am. A* 23 (2006) 3139–3149.
- [46] V. Andresen, S. Alexander, W.M. Heupel, M. Hirschberg, R.M. Hoffman, P. Friedl, Infrared multiphoton microscopy: subcellular-resolved deep tissue imaging, *Curr. Opin. Biotechnol.* 20 (2009) 54–62.
- [47] X. Wu, F. Yang, T. Ming, R.L. Xiong, P.N. Wang, J.Y. Chen, Au nanorods can be used for long-term cell imaging? *Appl. Phys. Lett.* 98 (2011).
- [48] M. Lippitz, M.A. van Dijk, M. Orrit, Third-harmonic generation from single gold nanoparticles, *Nano Lett.* 5 (2005) 799–802.
- [49] S.P. Tai, Y. Wu, D.B. Shieh, L.J. Chen, K.J. Lin, C.H. Yu, et al., Molecular imaging of cancer cells using plasmon-resonant-enhanced third-harmonic-generation in silver nanoparticles, *Adv. Mater.* 19 (2007) 4520–4521.
- [50] J.H. Gao, H.W. Gu, B. Xu, Multifunctional magnetic nanoparticles: design, synthesis, and biomedical applications, *Acc. Chem. Res.* 42 (2009) 1097–1107.